ELSEVIER

Contents lists available at ScienceDirect

Additive Manufacturing Letters

journal homepage: www.elsevier.com/locate/addlet



Short Communication

Rapid exploration of nanoparticle-modified alloys in metal additive manufacturing by combining inkjet printing and laser powder bed fusion

Emre Tekoglu^{a,b,†}, Shuheng Liao^{a,†}, Zachary Kutschke^a, Alexander D. O'Brien^b, Bethany Lettiere^a, Ju Li^{b,*}, A. John Hart^{a,*}

ARTICLE INFO

Keywords: High-throughput screening Nanoparticle-enhanced alloys Composition control Inkjet printing Laser powder bed fusion

ABSTRACT

The development of new metal alloys is key to the continued advances in critical technologies such as jet engines operating at higher temperatures, rocket engines with longer lifetime and reusability, and reactors for fusion and fission energy generation. While additive manufacturing (AM) is attractive for both prototyping and production of advanced alloys and components, the experimental screening and validation of new alloys typically requires costly synthesis of custom powder feedstocks. We present a technique for high-throughput screening of nanoparticle-enhanced alloys for AM, combining inkjet printing and laser powder bed fusion (LPBF). Alloyed specimens are prepared on metal substrates with shallow machined cavities; a nanoparticle-containing ink is printed into the cavities via inkjet deposition; powder is manually spread into the wells; and then the material is melted by scanning of a laser as in traditional LPBF. We exercise this workflow using Niobium as the base metal and with custom-formulated inks containing Si and/or Ti nanoparticles. The alloyed specimens exhibit locally defined composition, microstructure, and hardness. We demonstrate control of minority element composition of <1 % to >10 % over <1 mm distances, and along with the capability to create multi-material gradients exhibiting complex microstructural effects.

1. Introduction

The development of new metal alloys is key to the continued evolution of critical technologies such as jet engines operating at higher temperatures [1], rocket engines with longer lifetime and reusability [2], and reactors for fusion and fission energy generation [3]. Additive manufacturing (AM) is opening up the alloy design spectrum, for instance enabling new superalloy compositions with high gamma prime fraction [4], ceramic nanoparticle (NP) reinforced alloys [5,6], and high entropy alloys [7]. AM is especially attractive because traditional workflows such as casting and forging require much larger sample volumes and often necessitate dedicated tooling and heavy equipment. These attributes are incommensurate with high throughput characterization techniques. In contrast, the development of AM processes allows researchers to more efficiently customize tailored alloys based on composition, microstructure, and/or specific properties. Using AM to create combinatorial and gradient specimens can vastly increase the

amount of data that can be collected from a single sample batch, enabling the high throughput screening of new alloys.

Laser powder bed fusion (LPBF) has gained prominence among metal AM techniques due to its high dimensional accuracy and a wider selection of proven feedstock materials than other metal AM methods [8–10]. LPBF also holds great potential for creating compositionally graded parts, by localization of the laser for melting and controlled solidification, optionally combined with manipulation of the powder feedstock used for the build. One example of controlling solidification site-specifically is presented by Gao et al. [11], where different hatch spacing values were programmed in a single part to create a complex microstructure that combines recrystallized and non-recrystallized regions with different properties.

Further focusing on LPBF, several studies have demonstrated the capability to produce powders of various compositions and interchange these feed powders with layer height [12–14]. These works provide new levels of precision in exploring material compositional spaces and

E-mail addresses: liju@mit.edu (J. Li), ajhart@mit.edu (A.J. Hart).

^a Department of Mechanical Engineering, Massachusetts Institute of Technology, Cambridge, MA, 02139, USA

b Department of Nuclear Science and Engineering, Massachusetts Institute of Technology, Cambridge, MA, 02139, USA

^{*} Corresponding authors.

 $^{^{\}dagger}$ These authors contributed equally.

greatly expand the quantity of available data when transitioning between two discrete materials but remain limited to a unidirectional gradient following the part's build direction. For example, Demir et al. [14] used a dual hopper system to change the powder mixing ratio between layers and produce graded specimens varying from AISI 316 L to Fe35Mn gradually along the build direction. Systems have also been created to selectively deposit powders in certain regions on the build plate [15], but to the authors knowledge these are suitable mainly for abrupt changes in composition and cannot achieve fine programmed gradients.

Additionally, directed energy deposition (DED) AM processes have achieved multi-material control by varying the composition of the feedstock/powder being blown into the melt pool, such as demonstrated by Oropeza et al. [16] and Kelly et al. [17]. However, the DED process is fairly limited in terms of the dimensional precision and resolution achievable, given that the typical laser spot size in such a process is on the order of millimeters, and layer heights are usually in the range of 200–500 µm or greater [18]. Although geometric resolution may not be the primary consideration in early-stage alloy development, the more fundamental distinction between DED and LPBF the substantial difference in thermal gradients and solidification dynamics. Heating and cooling rates in LPBF are typically in the range of 10^4-10^7 K/s, compared to DED at 10²-10⁴ K/s due to larger melt pools and slower scan speeds [19]. These differences critically affect microstructural evolution, including grain morphology, segregation profiles, and the formation of secondary phases.

It is therefore of interest to consider other approaches that, when combined with LPBF, could achieve higher resolution of spatial composition, and eliminate the need for mixing multiple alloy powders. Inkjet printing, which is widely used in production of graphics and many other manufactured goods, can deposit droplets with diameters in the ~tens of micrometers at very high throughput owing to the parallelization of microfabricated nozzles (typically hundreds or thousands of nozzles in an industrial printhead) [20,21]. Inkjet printing is also widespread in AM, being used for single- and multi-material polymer AM, and for deposition of binder on to the powder bed in binder jetting. Using inks loaded with metallic nanoparticles, inkjet printing has been used to print simple circuits and circuit elements [22,23], and even small metal structures [24].

Recently, it has been shown that local deposition of liquid inks onto the powder bed in LPBF can be used to locally tailor material composition, by augmenting the process to accommodate layer-wise deposition along with layer-wise laser melting. For instance, Hesselmann et al. deposited carbon nanoparticle suspensions onto a stainless steel (410 L) powder bed [25]. They demonstrated local formation of microstructures composed of ferrite, martensite, and chromium-rich carbides, and corresponding local changes in hardness. In a parallel effort, Lee et al. [26] developed a hybrid LPBF process that uses jetting to deposit copper-laden nanoparticle ink. After LPBF and annealing, Cu-rich regions were formed within the SS316L alloy, increasing thermal conductivity up to 181 % (at 300 °C) relative to SS316L.

To advance this promising approach to high-resolution compositionally graded AM, it is necessary to understand the detailed relationships among process parameters, alloy composition, microstructure, and functional properties. Moreover, it is attractive to do so in a material-efficient manner that generates an array of compositions over limited specimen area and/or volume, which is an intrinsic advantage of inkjet printing. Here, we combine inkjet printing and LPBF on planar specimens to study the feasibility of inkjet-LPBF to create nanoparticle-enhanced alloys in AM. Our workflow involves deposition of nanoparticle-laden ink via inkjet printing on a substrate with a shallow cavity, followed by a conventional single-layer LPBF process to achieve in-situ production of metallic alloys with high-resolution composition control. We show how local specification of the ink concentration based on the droplet density and number of inkjet passes translates into precise spatial control of the alloy composition, enabling continuous or abrupt

transitions in printed composition by design.

For this study, we specifically selected Niobium-based (Nb-based) refractory alloys as a test case. AM of Nb is of interest because production of Nb-based alloys via traditional casting and forging techniques is especially challenging [27-32]. Moreover, Nb has attractive high temperature strength and creep resistance with relatively low density (8.6 g/cm³) compared to most refractory metals [27,33,34]. As such, the discovery of appropriate LPBF-compatible Nb alloy compositions is a high-value target which could greatly benefit from the application of high-throughput screening. In the present work, Titanium (Ti) and silicon (Si) NPs were added as alloying elements, and subsequent material characterization was performed to investigate their effects on microcracking, porosity, and microhardness. Ti was selected due to its ability to form solid solutions with Nb, improving strength while contributing to oxidation resistance [35]. Si was chosen for its known role in enhancing high-temperature oxidation resistance [29] and forming stable Nb-silicide phases that improve thermal and mechanical stability. These characteristics make both elements promising candidates for tailoring Nb-based alloys for high-performance applications.

2. Materials and methods

Fig. 1 shows the workflow applied to create single-layer compositionally graded specimens by inkjet-LPBF. As detailed below, inks containing nanoparticles with the selected alloying elements (Si and Ti) are selectively jetted onto a Nb substrate, which is then coated with a layer of Nb powder. Then the specimen is processed by laser melting, using a conventional LPBF system, to produce a spectrum of multiple compositions with depth comparable to a single layer in a three-dimensional LPBF process.

2.1. Substrate fabrication

Specimens are fabricated on Nb plates (6 mm thickness, Nexmetal Corp., 99.99 % purity) with shallow rectangular cavities (referred to as templates). The template depth is chosen to set the layer thickness of the deposited material (i.e., ink plus powder) while permitting manual powder spreading. The substrate is machined into a dog-bone geometry with an overall length of 75 mm, a gauge section width of 9 mm, and a gauge length of 55 mm. Within this gauge section, six shallow wells are machined, each with a depth of 50 µm and spatial dimensions 6 mm by 12 mm. The wells are spaced with a 3 mm gap between adjacent wells to prevent thermal interaction and ensure compositional isolation during LPBF processing. These cavities serve as defined regions for inkjet deposition, manual powder spreading, and subsequent laser melting. The templates are machined into the plate using a tungsten carbide end mill (3 flutes, 4.76 mm diameter) at 5000 RPM spindle speed and 12.7 cm/min feed rate. Prior to machining of the templates, the plate is cut into a dog-bone shape by wire electro discharge machining (EDM).

2.2. Ink formulation

Inks were formulated by combining selected NPs with deionized water (DI water), ethanol, and a solution of a copolymer (DISPERBYK-2018, BYK Company). The NPs were elemental Si (SkySpring Nano-MaterialsTM, 99.7 % purity, particle size ≤ 500 nm) and Ti (SkySpring Nano-MaterialsTM, 99.7 % purity, particle size ≤ 100 nm), shown in Figure S1a-b. The weight ratio between the DI water and ethanol was fixed to 4:1 as described by Dan et al. [36] to ensure proper surface energy and viscosity behavior of the liquid. Solutions consisting of 77.6 % DI water, 19.4 % Ethanol, and 1 wt % DISPERBYK-2018 was selected and mixed with 2 wt % of Si or Ti NPs. The inks were prepared in a glove box under 99.999 % purity argon (Linde, Marlborough, MA, USA). The inks were sonicated (CREST Ultrasonics 1100D, power 6 for 30 mins) to ensure adequate dispersion of the NPs prior to loading in the inkjet system.

Inkjet printing → (Powder spreading) → Laser melting a Laser scanning Piezoelectric Solidified transducer Powder alloy Nozzle ~0.2 mm NP Ink Plate with machined wells X-Y motors Camera Inkjet nozzle Ink reservoir Plate with machined wells 50 mm Z adjustment

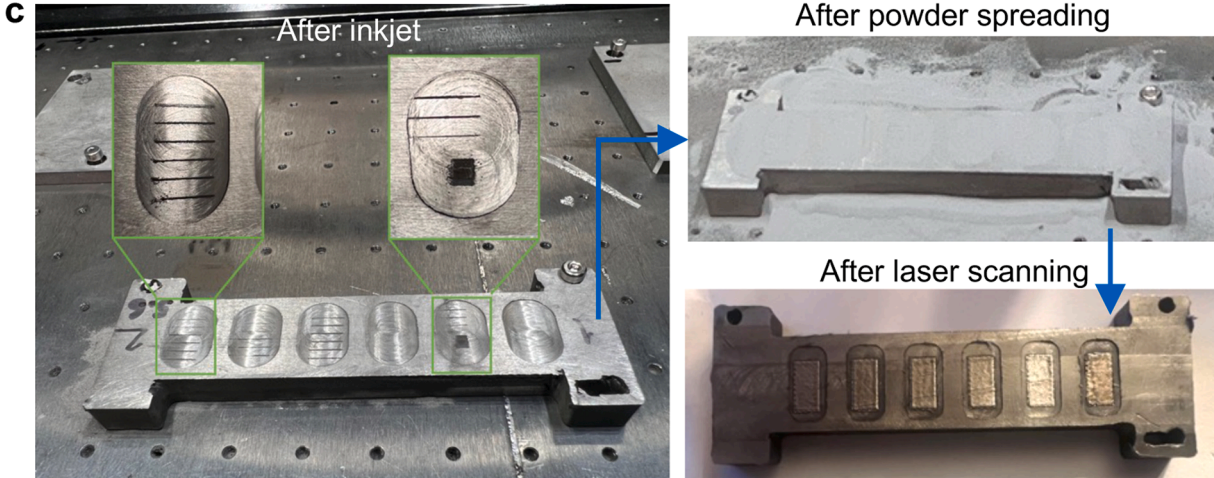


Fig. 1. (a) Workflow applied to create single-layer compositionally graded specimens by inkjet-LPBF, using a metal plate with machined wells; (b) Single-nozzle inkjet printing testbed, and close-ups of the nozzle and a stable droplet after ejection (right); (c) Key steps in creation of single-layer compositional graded alloy specimens. Powder was spread manually over the substrate and laser melting was performed using a commercial LPBF system with the substrate anchored to a conventional build plate.

2.3. Inkjet deposition

Inkjet deposition was performed using a custom-built testbed (Fig. 1b) that includes a piezoelectric drive controller (MicrofabTM Jet-Drive V, CT-M5–01), a piezoelectric dispensing nozzle with an 80 μm orifice diameter (MicrofabTM MJ-AT-01–080) and a digital pressure controller (APEXTM Vacuum LLC). Jetting was performed using a custom LabView program to control the jetting locations, nozzle traverse speed, jetting voltage and frequency. The optimized inkjetting conditions were as follows: 100 Hz jetting frequency, 10 mm/s jetting speed, 100 μm droplet spacing and 60 V jetting voltage. A 3-second dwell time was applied between each pass to allow for solvent leveling, and the printed samples were left to rest for over 1 hour prior to the LPBF step to ensure complete solvent evaporation. For an exemplary experiment, Fig. 1c

provides a representation of the process steps (i.e., after NP inkjetting, after Nb powder spreading, after LPBF) performed to print single-layer compositionally graded specimens by inkjet-LPBF.

2.4. Laser powder bed fusion

Following inkjet printing and solvent evaporation, powder is spread manually onto the substrates, filling the cavities. Gas atomized Nb powders (American ElementsTM, 99.9 % purity) were used, having a spherical particle morphology (Figure S1c). LPBF was then performed using a commercial system (EOS M290). In principle, the order of inkjet deposition and powder spreading can be reversed, i.e., the NP ink can be deposited onto the powder layer after spreading (analogous to binder jetting). However, due to limitations of the commercial LPBF system

used in this study, we deposited the ink prior to powder spreading. The scanning parameter set was determined based on preliminary LPBF tests of single layer pure Nb, giving the following: 250 W laser power, 400 mm/s scanning speed, 50 μm hatch spacing, 100 μm laser spot size. The chamber was maintained with Ar (99.9 %), and the substrate was not heated.

2.5. Characterization

Scanning electron microscopy (SEM) was performed using a Zeiss Merlin (Carl Zeiss AG, Oberkochen, Germany), equipped with an energy dispersive spectrometer (EDX) and electron back scatter diffraction (EBSD). Vickers microhardness was measured using a Struers/Emco-

Test DuraScan Automatic Hardness Tester (Struers LLC, Cleveland, OH, USA) under a load of 0.02 kg (0.20 N) for 10 s.

3. Results and discussion

To develop the inkjet-LPBF workflow, we first identified inkjet printing parameters that resulted in uniform, well-defined lines of ink on the metal (Nb) substrate. With the nozzle size and ink formulation fixed (see Methods), the jetting frequency (f) and linear speed (ν) must be chosen appropriately. With increasing speed at constant jetting frequency, the printed pattern transitions from isolated drops to a continuous line to a bulged line, as shown in Fig. 2a. As viewed in SEM/EDX (Fig. 2b), representative isolated and bulged patterns give non-uniform

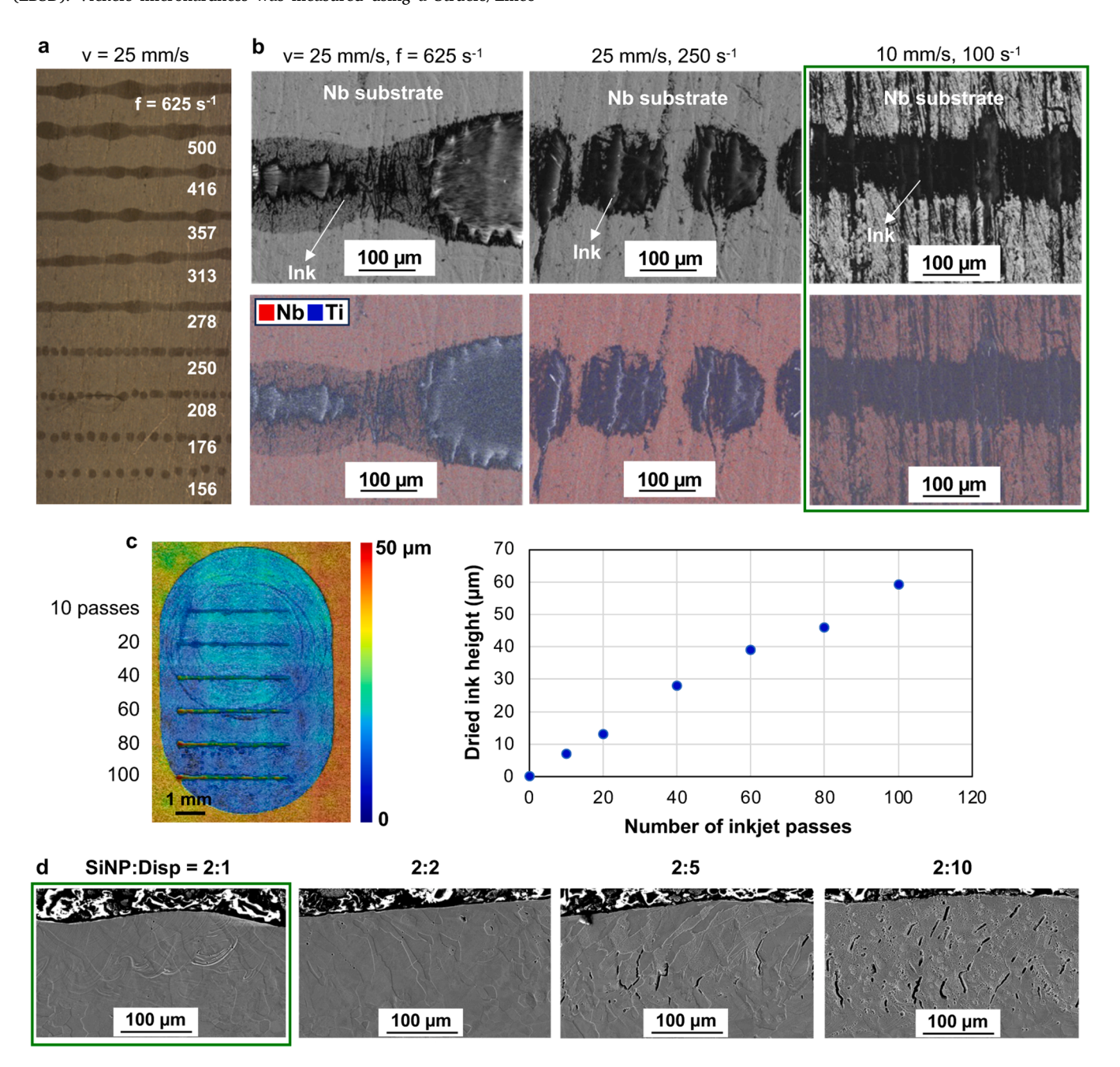


Fig. 2. (a) Development of inkjet print parameters for Ti NP inks; pattern transitions from isolated drops to a continuous line to a bulged line when printing at increasing drop frequency and constant translation speed; (b) SEM and EDX results showing evolution of printed patterns with Ti NP inks with respect to different inkjet conditions; (c) Surface height color map and plot showing relationship between the height of the printed Ti NP lines and the number of inkjet passes; (d) Cross-sectional SEM images of the specimen printed with different amounts of organic dispersant included in Si the NP ink (laser scanning direction perpendicular to the cross-section).

deposits (after solvent evaporation), whereas continuous lines have much more uniform height indicated by the intensity of the Ti signal in the image. From these tests, $f=100~\mathrm{Hz}$ and $\nu=10~\mathrm{mm/s}$ were chosen as inkjet parameters going forward.

Multiple inkjet passes must be printed to tailor the local quantity of nanoparticles and therefore present significant local variation of the alloy composition. To enable calibration of the relative amounts of additive relative to the base alloy, we measure the relationship between the height of the printed lines and the number of passes, giving the approximately linear relationship shown in Fig. 2c-d. The height profile of the dried ink increases with each consecutive pass, owing to deposition of the Ti-NPs. The thickness of the dried ink strips is proportional to the number of inkjet passes, approximately 500 nm per pass, after drying. At 40 passes the dried ink is approximately 25 µm thick, which is almost half of the template depth. With more passes (i.e., 60, 80, 100), the thickness of the ink strip fills most of the template depth, yet good mixing of the additive and Nb is found in the final alloy, indicating that the material homogenizes locally upon melting and solidification. While SEM/EDX characterization in Fig. 2b illustrates the lateral uniformity achieved with single-pass deposition, subsequent passes primarily thicken the ink deposition rather. The ink lines retain a consistent width $(\sim 200 \mu m)$ even at high pass numbers due to the stabilizing effects of surface tension and substrate wetting, as supported by surface height

measurements and cross-sectional SEM/EDX analyses (Figs. 3d and4c).

Following inkjet printing, Nb powder is spread manually over the cavities containing the printed ink patterns, and LPBF is performed by aligning the specimen to the scan pattern within the LPBF system. Initial tests revealed the importance of balancing the ink formulation to maintain adequate dispersion of the NPs, avoiding settling in the vial while printing, while limiting the concentration of organic dispersant. In fact, we found that higher levels of dispersant led to significant cracks and porosity as viewed in cross-sectional images of the specimens after the complete inkjet-LPBF workflow (Fig. 2d). Therefore, the final ink formulation (see Methods) with a weight ratio of 2:1 NPs:dispersant was chosen. Ethanol, having a low boiling point, is expected to evaporate under ambient conditions prior to powder spreading. The organic dispersant, is expected to decompose during the LPBF laser melting step. Although direct measurements of carbon content were not performed in this study, SEM/EDX analysis did not reveal the presence of carbon-rich secondary phases, and fully dense microstructures were observed in specimens fabricated using the optimized ink formulation (see Fig. 2d). The consistency of microhardness values and microstructure with known Nb-Si and Nb-Ti alloy systems suggests that any residual carbon content is minimal. Nevertheless, future work involving direct quantification of light elements such as carbon (e.g., via LECO or SIMS analysis) is necessary to confirm the extent of removal of organics, which is

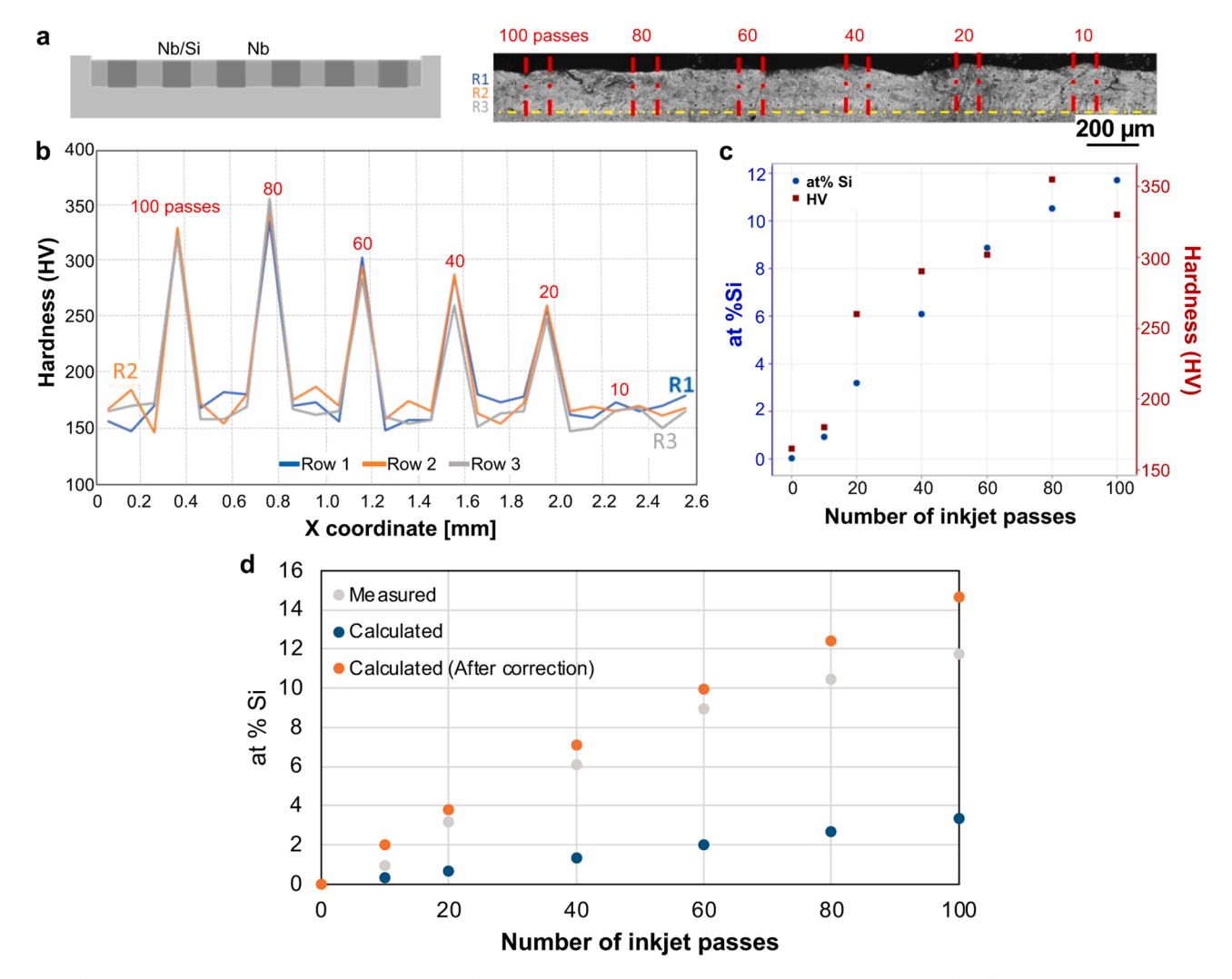


Fig. 3. (a) Illustration and cross-section SEM image of single-layer compositionally graded Nb/Si specimen by inkjet-LPBF; hardness test was performed on three rows (R1, R2, R3); (b) Microhardness profile of the specimen, where X coordinate in panel corresponds to horizontal position across the specimen cross-section; (c) Measured relationships between number of inkjet passes and Si loading (at %, left axis) and hardness (right axis); (d) comparison of predicted and measured Si loadings, versus number of inkjet passes.

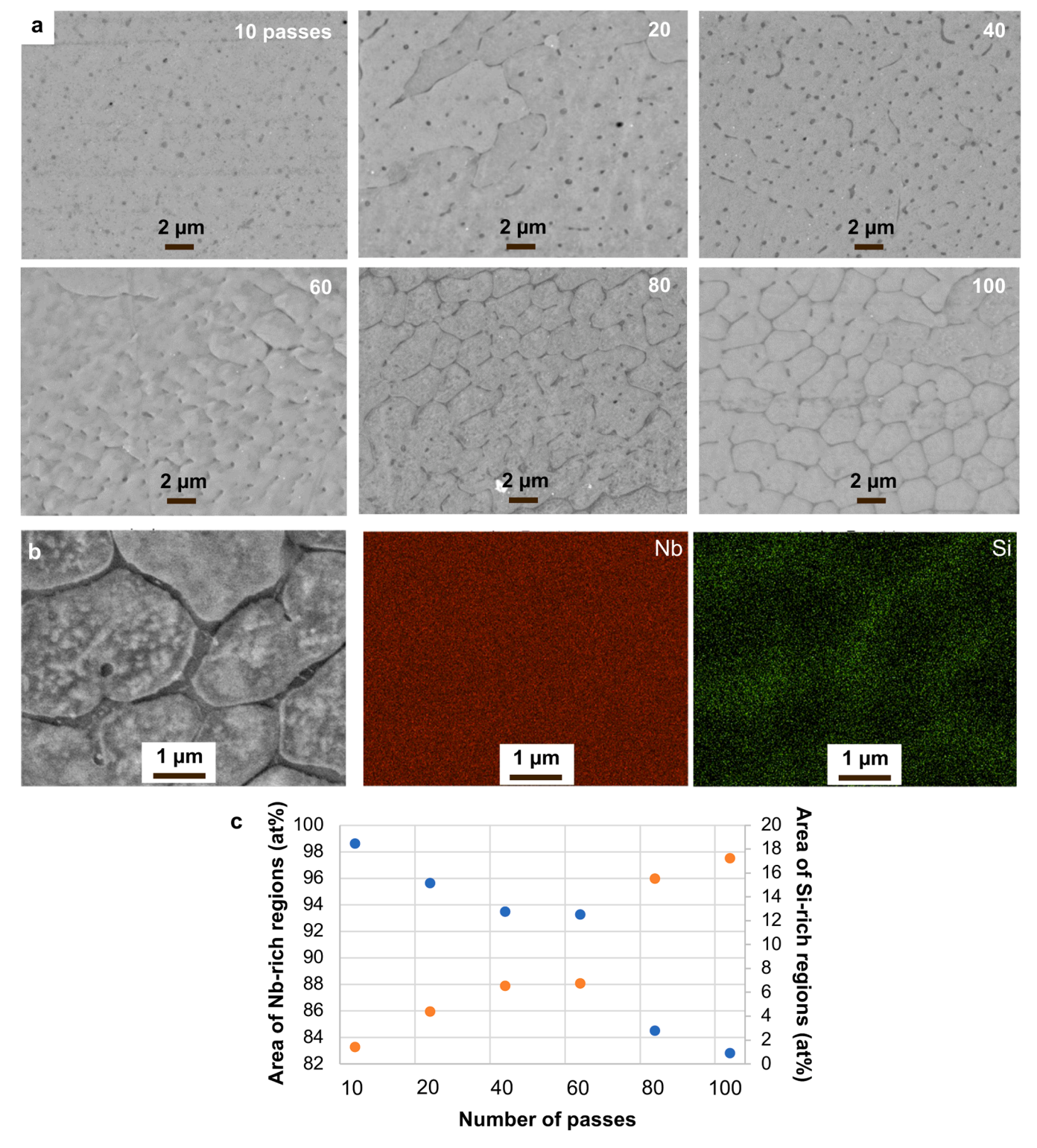


Fig. 4. (a) Cross-sectional SEM images of the areas loaded with Si concentrations show distinct changes in cellular sub-grains, with intergranular darker Si-rich regions (laser scanning direction perpendicular to the cross-section); (b) High-magnification SEM and EDX images from the Nb/Si region fabricated with 100 inkjet passes; (c) Variation in area fraction of Nb-rich (left axis) and Si-rich (right axis) regions.

important to the utility of this approach for high-precision alloy screening.

In the samples with higher dispersant content, we hypothesize that the cracks and pores may be due to inhomogeneity in the feedstock composition, and/or due to gas generation from rapid decomposition of the dispersant residue upon heating. In situ gas generation has been exploited to create porous components by LPBF, by bulk mixing of

foaming agents mixed with the feedstock powder [37,38]. While the porous samples suggest yet another means of local control imparted by inkjet, foregoing experiments focused on the ink formulation and process parameters to achieve fully dense cross-sections. This also minimized the likelihood of organic residue within the alloy, while using enough dispersant to maintain ink stability for jetting.

From this point, the tailored ink formulation and inkjet parameters

were used to create planar alloy specimens with spatially graded composition, combining the Nb substrate with Nb powder, and locally deposited Si and/or Ti NPs that mixed into the melt track upon laser scanning over the powder-filled templates. For instance, we modulated the composition in a manner that gave a sequentially increasing Si concentration in Nb, by printing isolated, parallel lines of Si NPs with an increasing number of inkjet passes (10, 20, 40, 60, 80, and 100 passes), as shown in Fig. 3c. Moving from left to right with respect to the presented cross-section (Fig. 3a-b), the hardness (measured perpendicular to the surface of the cut section) oscillates between the baseline value of pure Nb and increasing values corresponding to a higher loading of Si, which was dictated by the quantity of Si NP ink printed in the corresponding locations prior to powder spreading and laser melting (Fig. 3c). In the unmelted regions of the cross-section (pure, as-obtained Nb), the hardness is 80–100 HV which corroborates literature [39,40],

and the Si-modified Nb hardness reaches a maximum of 354 HV in the area where 80 inkjet passes were applied (16–18 wt % Si). The area with 100 inkjet passes has a slightly higher measured Si loading, but lower hardness, as we possibly reached the maximum loading dictated by the geometric confinement of the ink (i.e., total line height) and the template depth which must also accommodate powder.

After LPBF, this striped inkjet pattern leads to well-defined regions, viewed in cross-section, with varying Si content, microhardness, and microstructure. Cross-sectional SEM images of the areas loaded with different ink concentrations show distinct concentration of Si in Nb matrix (Fig. 4a); where the darker regions show higher Si concentration. The microstructure of the Nb/Si region is consistent with Nb-Si based alloys studied in the literature where a dual phase microstructure consists of Nb-based solid solution and Nb silicides [29]. In the inkjet-modified sample, at lower Si concentrations, Si-rich phases were

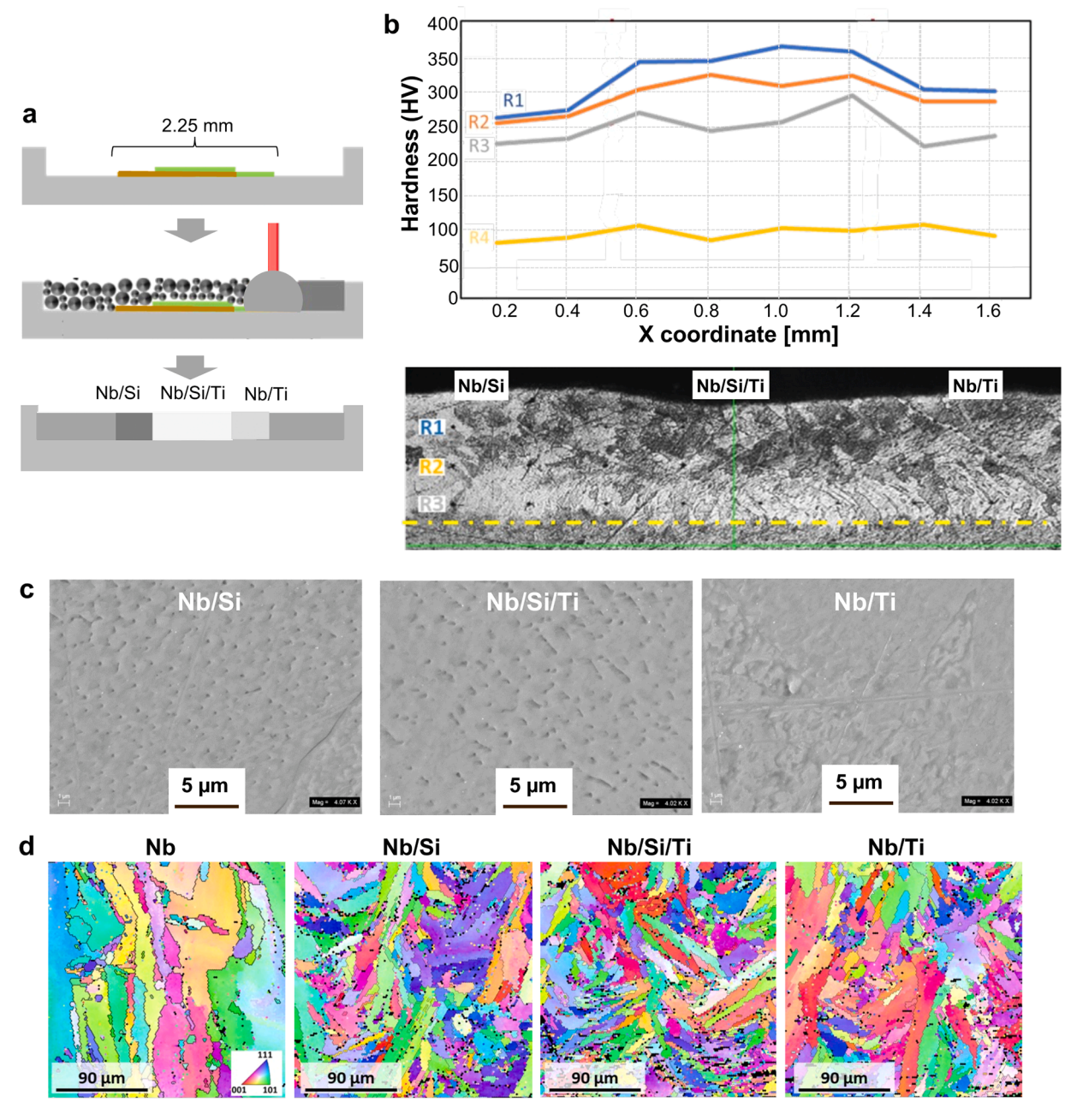


Fig. 5. (a) Workflow applied to create single-layer compositionally graded Nb/Si/Ti specimen by inkjet-LPBF; (b) Microhardness profile of cross-section of Nb/Si/Ti specimen; (c) Corresponding cross-sectional SEM images of Nb/Si, Nb/Si/Ti and Nb/Ti regions; (d) EBSD orientation maps showing spatial variation in grain size and orientation.

in the form of precipitates whereas at higher Si concentrations the related phase region formed an interconnected network phase structure in the Nb alloy (Fig. 4b). The area fraction of the Si-rich phase, measured by analysis of the SEM images, reached up to 16-18 % at 80 and 100 inkjet passes (Fig. 4c). The area fractions of Nb-rich and Si-rich phases shown in Fig. 4c were evaluated through image analysis of cross-sectional SEM micrographs. The images were converted to gravscale and thresholded using ImageJ software to distinguish the Si-rich phase (which appears darker) from the Nb-rich matrix. The binary images were analyzed using ImageJ to calculate the percentage of the area occupied by the segmented Si-rich regions relative to the total image area. Altogether, the examined cross-section was free of microporosity and cracking, and the composition is uniform in the lateral direction of the cross-section. We observe that vertical mixing within the melt pool is limited to a relatively shallow region, and this requires further understanding as discussed later.

Next, we show the capability of the inkjet-LPBF technique to combine multiple elemental inks to achieve more complex alloy compositions with local control. Overlapping inkjet printed regions with Sibased and Ti-based NP inks, respectively, yields a post-LPBF composition graded from Nb to Nb/Si, Nb/Si/Ti, Nb/Ti, and Nb (Fig. 5a). Corresponding cross sectional SEM images of Nb/Si and Nb/Si/Ti regions (Fig. 5c) show dual phase regions like those observed in the Nb/Si sample above. The Nb/Ti region only shows a single-phase region, which is most likely a Nb-Ti solid solution. The microhardness of the Nb/ Si region is 220-260 HV, the Nb/Si/Ti region is 240-360 HV, and the Nb/Ti region is 220-300 HV (Fig. 5b). EBSD images reveal smaller grain sizes in the Nb/Si, Nb/Si/Ti and Nb/Ti, compared to the pure Nb in the region that was laser melted (Fig. 5d). On the other hand, as displayed in Figure S2, Nb showed a higher fraction of low angle boundaries (0–5°) compared to the alloy regions; therefore, we conclude that incorporation of Si and Ti NPs into Nb favored grain refinement and formation of high angle grain boundaries, in a locally defined manner.

Importantly, the microstructures observed in high-magnification SEM images (Fig. 5c) correspond to cellular sub-grains, which typically form during rapid solidification in LPBF. These structures often appear in the order of a few microns and are governed by local thermal gradients and solidification rates. In contrast, the grain sizes quantified in the EBSD maps (Fig. 5d) represent crystallographic grains, measured using the Feret diameter approach, which provides a reliable estimate of maximum grain length. The data show characteristic grain sizes approaching $\sim\!100~\mu m$ in the pure Nb region, while significantly smaller grain sizes are observed in the alloyed regions. This reduction in grain size confirms that alloying with Si and Ti promotes grain refinement, likely due to solute effects on nucleation and growth, along with high thermal gradients during solidification. Thus, EBSD provides a more accurate and quantitative assessment of grain evolution compared to surface morphology alone.

An important consideration for the applicability of the inkjet-LPBF technique in achieving designed alloy compositions is the accuracy with which the final (post-LPBF) composition can be predicted from the amount of deposited ink relative to the amount of base alloy available in the melt region. In the case of the Nb-Si specimen, the expected Si concentration is calculated as

$$C_{\text{Si}} = \frac{\frac{m_{\text{Si}}}{M_{\text{Si}}}}{\frac{m_{\text{Si}}}{M_{\text{Si}}} + \frac{m_{\text{Nb}}}{M_{\text{Nb}}}}$$
(1)

where $C_{\rm Si}$ is the concentration of Si in atom percent (at%), $m_{\rm Si}$ and $m_{\rm Nb}$ are the mass of Si and Nb in the alloy region. The molar mass of Si and Nb are denoted by $M_{\rm Si}$ and $M_{\rm Nb}$, respectively. The mass of Si is calculated from the total volume of ink droplets and the concentration of the NPs:

$$m_{\rm Si} = \frac{4}{3}\pi \left(\frac{d}{2}\right)^3 * N * \frac{Lf}{\nu} * \rho_{\rm ink} * w_{\rm NP}$$
 (2)

where d is the diameter of the nozzle (80 μ m), N is the number of inkjet passes, , f is the jetting frequency (100 Hz), v is the jetting speed (10 mm/s), L is the length of the ink line, $\rho_{\rm ink}$ is the density of the ink and $w_{\rm NP}$ is the weight ratio of NPs in the ink (2 wt %). The mass of Nb in the alloy region is calculated by

$$m_{\rm Nb} = \rho_{\rm Nb} * D * W * L \tag{3}$$

where $\rho_{\rm Nb}$ is the density of Nb, W and D are the width and depth of the alloy region. Here we simply approximate W by the width of the ink line (~200 μ m) and D by the expected depth of the melt pool (~300 μ m).

In Fig. 3d we compare the predicted and measured Si concentration values. The measured Si concentration is significantly higher than the predicted values. One major possible reason, which has been verified in ongoing work performing full three-dimensional printing using the inkjet-LPBF technique, is that the NPs are not uniformly distributed along the vertical direction in the melt pool and are concentrated mostly within the top region of the melt pool. In single-layer experiments an abrupt transition in composition is observed when traversing vertically downward through the melt pool, and therefore uniform composition is assumed above this location. To account for the limited penetration, we applied a correction factor to the depth of the alloy region:

$$m_{\rm Nb} = \rho_{\rm Nb} * c * D * W * L \tag{4}$$

In the current work we assume c=0.25, i.e., D is equal to 25 % of the melt pool depth (~75 μ m) which is slightly greater than the template depth. After application of this uniform correction, the predicted Si concentrations are close to the measured values (error < 1 at %), as shown in Fig. 3d Further work is necessary to assess the spatial composition of the melt pool, and the influence of the scan pattern and trajectory parameters (e.g., raster strategy, hatch spacing, melt depth) on the final composition distribution and implications for spatial control both laterally and vertically.

The ratio of the measured versus expected (based on ink composition) loading of Si and Ti in the final specimen appears to depend on the absolute amounts of each, suggesting that it is not straightforward to predict the final composition in advance. However, calibration of the technique along with production of samples with a range of compositions still affords high throughput screening. The achievable incremental and maximum loadings can be determined for specific material combinations, and further studies can elucidate the spatial resolution of composition grading as related to the melt pool geometry and nature of interaction (e.g., dissolution, precipitation, or other effects) between the NP additives and the base powder that is mixed during LPBF. The spatial resolution is also influenced by the drop size, powder size and packing density, and layer thickness, and requires detailed investigation in future work with exemplary alloy systems.

4. Conclusion

We showed that inkjet printing provides a versatile means of spatially tailoring the feedstock composition suitable for creating nanoparticle-enhanced alloys in LPBF. Using single-layer template substrates and Nb alloys to inform a model system, we showed that the inkjet-LPBF approach can fabricate, with sub-mm spatial resolution, single- and dual-NP-modified Nb alloys, wherein the local composition is tailored by the number of inkjet passes, and the alloys show uniform local composition and microstructure without voids. Looking forward, this approach can be extended to other alloys for various uses (e.g., grading carbon composition in steels, creating new refractory alloys) and specialized ink formulations. In addition, ongoing work is focused on scaling the process to enable full three-dimensional spatial grading, which requires layer-to-layer alignment of printed ink patterns, control of ink infiltration and drying kinetics, understanding of the mixing of additives within the melt pool and between tracks/layers, and integration with layer-wise LPBF scanning strategies. Ultimately realizing the

inkjet-LPBF process in full 3D printing will extend the rapid material exploration capability to macroscopic specimens amenable to conventional mechanical testing and enable architected, compositionally graded components with application-specific microstructural and functional properties.

CRediT authorship contribution statement

Emre Tekoglu: Writing – review & editing, Writing – original draft, Validation, Methodology, Investigation, Conceptualization. Shuheng Liao: Writing – review & editing, Writing – original draft, Validation, Methodology, Investigation. Zachary Kutschke: Writing – review & editing, Investigation. Alexander D. O'Brien: Writing – review & editing, Investigation. Bethany Lettiere: Writing – review & editing, Methodology. Ju Li: Writing – review & editing, Supervision, Funding acquisition. A. John Hart: Writing – review & editing, Writing – original draft, Supervision, Methodology, Funding acquisition, Conceptualization.

Declaration of competing interest

The authors declare that they have no known competing financial interests or personal relationships that could have appeared to influence the work reported in this paper.

Acknowledgements

Financial support was provided by the Advanced Research Projects Agency-Energy (ARPA-E, Award Number DE-AR0001434. A.D.O. acknowledges support of the National Science Foundation Graduate Fellowship Award #4999143677. We thank Dave Follett (UMass Amherst) for assistance with LPBF processing. This work also used shared characterization facilities at MIT.nano.

Supplementary materials

Supplementary material associated with this article can be found, in the online version, at doi:10.1016/j.addlet.2025.100315.

Data availability

Data will be made available on request.

References

- [1] Y. Wan, Y. Cheng, Y. Chen, Z. Zhang, Y. Liu, H. Gong, B. Shen, X. Liang, A. Nitride-Reinforced, NbMoTaWHfN refractory high-entropy alloy with potential ultra-high-temperature engineering applications, Engineering 30 (2023) 110–120.
- [2] P.R. Gradl, C.S. Protz, D.L. Ellis, S.E. Greene, Progress in additively manufactured copper-alloy GRCop-84, GRCop-42, and bimetallic combustion chambers for liquid rocket engines, Int. Astronaut. Congr. (IAC) (2019).
- [3] K. Ehrlich, Materials research towards a fusion reactor, Fusion Eng. Des. 56 (2001) 71–82.
- [4] H. Xiao, P. Xie, M. Cheng, L. Song, Enhancing mechanical properties of quasicontinuous-wave laser additive manufactured Inconel 718 through controlling the niobium-rich precipitates, Addit. Manuf. 34 (2020) 101278.
- [5] E. Tekoglu, A. O'Brien, J. Liu, B. Wang, S. Kavak, Y. Zhang, S. Kim, S. Wang, D. Agaogulları, W. Chen, Strengthening additively manufactured Inconel 718 through in-situ formation of nanocarbides and silicides, Addit. Manuf 67 (2023) 103478, 2023.
- [6] M.-Y. Shen, X.-J. Tian, D. Liu, H.-B. Tang, X. Cheng, Microstructure and fracture behavior of TiC particles reinforced Inconel 625 composites prepared by laser additive manufacturing, J. Alloys Compd. 734 (2018) 188–195.
- [7] J. Ren, Y. Zhang, D. Zhao, Y. Chen, S. Guan, Y. Liu, L. Liu, S. Peng, F. Kong, J. D. Poplawsky, Strong yet ductile nanolamellar high-entropy alloys by additive manufacturing, Nature 608 (7921) (2022) 62–68.
- [8] X. Zhang, C.J. Yocom, B. Mao, Y. Liao, Microstructure evolution during selective laser melting of metallic materials: a review, J. Laser Appl. 31 (3) (2019).
- [9] E.O. Olakanmi, R.F. Cochrane, K.W. Dalgarno, A review on selective laser sintering/melting (SLS/SLM) of aluminium alloy powders: processing, microstructure, and properties, Prog. Mater. Sci. 74 (2015) 401–477.

- [10] C.Y. Yap, C.K. Chua, Z.L. Dong, Z.H. Liu, D.Q. Zhang, L.E. Loh, S.L. Sing, Review of selective laser melting: materials and applications, Appl. phys. rev. 2 (4) (2015).
- [11] S. Gao, Z. Li, S. Van Petegem, J. Ge, S. Goel, J.V. Vas, V. Luzin, Z. Hu, H.L. Seet, D. F. Sanchez, Additive manufacturing of alloys with programmable microstructure and properties, Nat. Commun. 14 (1) (2023) 6752.
- [12] W. Li, X. Chen, L. Yan, J. Zhang, X. Zhang, F. Liou, Additive manufacturing of a new Fe-Cr-Ni alloy with gradually changing compositions with elemental powder mixes and thermodynamic calculation, Int. J. Adv. Manuf. Technol. 95 (2018) 1013–1023
- [13] C. Haase, F. Tang, M.B. Wilms, A. Weisheit, B. Hallstedt, Combining thermodynamic modeling and 3D printing of elemental powder blends for highthroughput investigation of high-entropy alloys–Towards rapid alloy screening and design, Mater. Sci. Eng.: A 688 (2017) 180–189.
- [14] A.G. Demir, J. Kim, F. Caltanissetta, A.J. Hart, C.C. Tasan, B. Previtali, B. M. Colosimo, Enabling multi-material gradient structure in laser powder bed fusion, J. Mater. Process. Technol. 301 (2022) 117439.
- [15] J. Walker, J.R. Middendorf, C.C. Lesko, J. Gockel, Multi-material laser powder bed fusion additive manufacturing in 3-dimensions, Manuf. Lett. 31 (2022) 74–77.
- [16] D. Oropeza, S. Firdosy, D.C. Hofmann, Development of in-plane SS316 to M300 maraging steel gradients via directed energy deposition, Addit. Manuf. Lett. 3 (2022) 100078
- [17] J. Kelly, J. Elmer, F. Ryerson, J. Lee, J. Haslam, Directed energy deposition additive manufacturing of functionally graded Al-W composites, Addit. Manuf. 39 (2021) 101845.
- [18] S. Gruber, C. Grunert, M. Riede, E. López, A. Marquardt, F. Brueckner, C. Leyens, Comparison of dimensional accuracy and tolerances of powder bed based and nozzle based additive manufacturing processes, J. Laser Appl. 32 (3) (2020).
- [19] Y.Z. Lek, C. Wang, X. Shen, Z. Chen, U. Ramamurty, K. Zhou, Additive manufacturing of corrosion-resistant maraging steel M789 by directed energy deposition, Mater. Sci. Eng.: A 857 (2022) 144032.
- [20] B. Derby, Inkjet printing of functional and structural materials: fluid property requirements, feature stability, and resolution, Annu Rev. Mater. Res. 40 (1) (2010) 395–414.
- [21] T. Cao, Z. Yang, H. Zhang, Y. Wang, Inkjet printing quality improvement research progress: a review, Heliyon 10 (10) (2024).
- [22] Y. Guo, H.S. Patanwala, B. Bognet, A.W. Ma, Inkjet and inkjet-based 3D printing: connecting fluid properties and printing performance, Rapid. Prototyp. J. 23 (3) (2017) 562–576.
- [23] E. Saleh, F. Zhang, Y. He, J. Vaithilingam, J.L. Fernandez, R. Wildman, I. Ashcroft, R. Hague, P. Dickens, C. Tuck, 3D inkjet printing of electronics using UV conversion, Adv. Mater. Technol. 2 (10) (2017) 1700134.
- [24] S.H. Ko, J. Chung, N. Hotz, K.H. Nam, C.P. Grigoropoulos, Metal nanoparticle direct inkjet printing for low-temperature 3D micro metal structure fabrication, J. Micromech. Microeng. 20 (12) (2010) 125010.
- [25] M. Hesselmann, R. Fechte-Heinen, L. M\u00e4dler, M. Steinbacher, A. Toenjes, Smartalloying-Liquid in-situ re-alloying in additive manufacturing, Addit. Manuf. 80 (2024) 103988.
- [26] K. Lee, V.V.K. Doddapaneni, S. Mirzababaei, S. Pasebani, C.-H. Chang, B.K. Paul, Multi-metal additive manufacturing of selectively doped 316 L stainless steelcopper composite using hybrid laser powder bed fusion, Addit. Manuf. 86 (2024) 104202.
- [27] P. Mastanaiah, G.M. Reddy, K.S. Prasad, C. Murthy, An investigation on microstructures and mechanical properties of explosive cladded C103 niobium alloy over C263 nimonic alloy, J. Mater. Process. Technol. 214 (11) (2014) 2316–2324
- [28] J. Chen, W. Ding, Q. Tao, C. Ma, C. Zhang, G. Chen, M. Qin, X. Qu, Laser powder bed fusion of a Nb-based refractory alloy: microstructure and tensile properties, Mater. Sci. Eng.: A 843 (2022) 143153.
- [29] Y. Guo, L. Jia, B. Kong, F. Zhang, J. Liu, H. Zhang, Improvement in the oxidation resistance of Nb-Si based alloy by selective laser melting, Corros. Sci. 127 (2017) 260–269
- [30] C.A. Terrazas, J. Mireles, S.M. Gaytan, P.A. Morton, A. Hinojos, P. Frigola, R. B. Wicker, Fabrication and characterization of high-purity niobium using electron beam melting additive manufacturing technology, Int. J. Adv. Manuf. Technol. 84 (2016) 1115–1126.
- [31] Z. Sun, F. Bao, F. Zhang, Y. Li, M. Wang, X. Guo, Effect of TiC on microstructures and mechanical behaviors of low-density Nb-Ti-Al alloys fabricated by laser solid forming, Int. J. Refract. Met. Hard Mater. 108 (2022) 105955.
- [32] Y. Guo, L. Jia, B. Kong, S. Zhang, F. Zhang, H. Zhang, Microstructure of rapidly solidified Nb-based pre-alloyed powders for additive manufacturing, Appl. Surf. Sci. 409 (2017) 367–374.
- [33] I.-T. Hong, C.-H. Koo, The study of vacuum-furnace brazing of C103 and Ti-6Al-4V using Ti-15Cu-15Ni foil, Mater. Chem. Phys. 94 (1) (2005) 131-140.
- [34] R. Grill, A. Gnadenberger, Niobium as mint metal: production-properties-processing, Int. J. Refract. Met. Hard Mater. 24 (4) (2006) 275–282.
- [35] A.J. Samin, Oxidation thermodynamics of Nb-Ti alloys studied via first-principles calculations, J. Alloys Compd. 879 (2021) 160455.
- [36] D. Oropeza, A.J. Hart, A laboratory-scale binder jet additive manufacturing testbed for process exploration and material development, Int. J. Adv. Manuf. Technol. 114 (11) (2021) 3459–3473.
- [37] D.-s. Shim, Effects of process parameters on additive manufacturing of aluminum porous materials and their optimization using response surface method, J. Mater. Res. Technol. 15 (2021) 119–134.

- [38] Y. Kathuria, Laser assisted aluminum foaming, Surf. Coat. Technol. 142 (2001)
- [39] S. Brunatto, A. Allenstein, C. Allenstein, A. Buschinelli, Cavitation erosion behaviour of niobium, Wear. 274 (2012) 220–228.
- [40] B.O. Shahreza, M.A. Hernandez-Rodriguez, E. Garcia-Sanchez, L. Kommel, F. Sergejev, A. Salinas-Rodríguez, A. Heczel, J. Gubicza, The impact of microstructural refinement on the tribological behavior of niobium processed by Indirect extrusion angular pressing, Tribol. Int. 167 (2022) 107412.